



Nanolead-Free Solder Pastes for Low Processing Temperature Interconnect Applications in Microelectronic Packaging

5

Hongjin Jiang, Kyoung-sik (Jack) Moon, and C. P. (Ching-Ping) Wong

Solder has long played an important role in the assembly and interconnection of integrated circuit (IC) components on substrates, i.e., ceramic or organic printed circuit boards. This type of alloy can provide electrical, thermal, and mechanical connections in electronic assemblies. Although the electronics industry has made considerable advances over the past few decades, the essential requirements of communications among all types of components in all electronic systems remain unchanged. Components need to be electrically connected for power and ground as signal transmissions. Tin/lead (SnPb) solder alloy has been the de facto interconnect material in most areas of electronic packaging, including interconnection technologies such as pin-through hole (PTH), surface-mount technology (SMT), ball grid array (BGA) (Fig. 5.1), chip scale packaging (CSP), and flip chip.

There are increasing concerns nowadays about the use of tin/lead alloy solders. Lead, a major component in solder, has long been recognized as a health threat to human beings. The major concern is that lead from discarded consumer electronics products in landfills could leach into underground water and eventually into drinking water system [1]. According to the latest report (US Geological Survey, Jan 2009), the total lead consumption by the US industries was 1,620,000 tons in 2008, a significant amount of which was used to produce alloy solders. Worst of all, most of the electronic products have a very short service life (e.g., cell phones, pagers, electronic toys, PDA), which often end up in landfills in just a few months or years. Recycling of lead-containing consumer electronic products has been proven to be very difficult, compared to that of lead-containing batteries or cathode-ray tube (CRT) displays.

The attempt to ban lead from electronic solder was initiated in the US Congress in 1990; however, the lead-free movement has advanced much more rapidly in Japan and Europe. The leading Japanese original equipment manufacturers (OEMs) have already introduced products that contain no lead in the interconnection. Although the WEEE (Waste Electrical and Electronic Equipment) Directive has put the European Union's lead-free legislation back to 2006, many companies such as Ericsson, Nokia, and Philips have already implemented "green" marketing strategies into their new products. These differences in lead-free progress have triggered great concerns about maintaining business opportunity among users of lead-containing solders, as such; it further expedites the advancement of lead-free soldering programs. Hence, lead-free electronics are not only perceived as a health issue, but their development is also driven by governmental and commercial interests. Many IC chip and board manufacturers including Intel, the largest microprocessor manufacturer, claim that their lead-containing products would be phased out around 2006.

A variety of lead-free solder alloys have been investigated as potential replacements for tin/lead solders. The main requirement for a lead-free solder alloy are

1. Low melting point: The melting point should be low enough to avoid thermal damage to the packages and high enough for the solder joint to bear the operating temperature. The solder should retain adequate mechanical properties at these temperatures:
2. Wettability: The solder materials should wet the base metal properly to provide the electrical, thermal, and mechanical connections between chips and substrates.
3. Availability and cost: There should be adequate supplies and at the same time the cost should be reasonable. The microelectronics industry is extremely cost conscious. The electronic manufactures are unlikely to change to an alternative solder material with an increased cost unless it has

H. Jiang (✉)

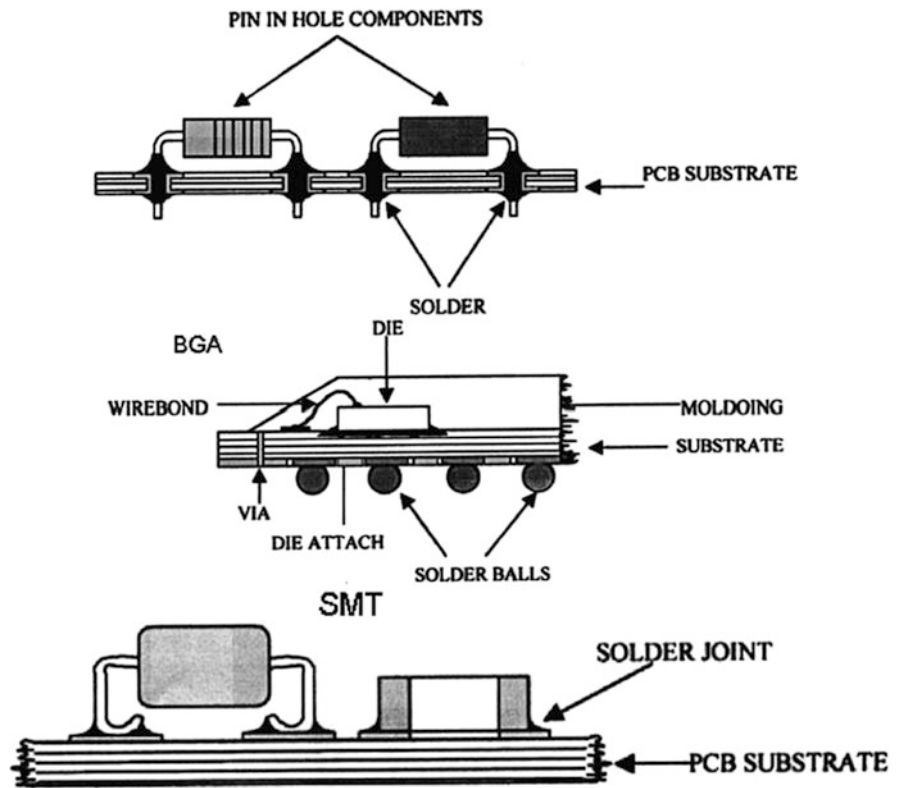
Intel Corporation, Chandler, AZ, USA

K. Moon · C. P. Wong

School of Materials Science and Engineering, Georgia Institute of Technology, Atlanta, GA, USA

e-mail: jack.moon@gatech.edu; cp.wong@mse.gatech.edu

Fig. 5.1 Schematic structures of pin-through hole (PTH), ball grid array (BGA), and surface-mount technology (SMT) packages using solder interconnects



demonstrated better properties or there is legislative pressure to do so.

Although several commercial and experimental Sn-based lead-free solder alloys exist, none can meet all the above requirements, especially if the melting point of the candidate alloys is required to be very close to that of the SnPb. Lead-free candidates and their respective melting points are listed in Table 5.1. Two alloy families, tin/silver/copper (SnAgCu) and tin/copper (SnCu), seem to be generating the most interest. SnAgCu alloy composition (with or without the addition of a fourth element) appears to be the most popular replacement and has been chosen to be the benchmark, with SnPb being the baseline, that all other potential alloys for the industry to be tested against. Concerns with this alloy family include higher processing temperatures, poorer wettability due to their higher surface tension, and their compatibility with lead-bearing finishes. The SnCu alloy composition is a low-cost alternative for wave soldering and is compatible with most lead-bearing finishes. Process considerations must be addressed with this alloy due to its higher melting temperature than most SnAgCu alloys.

As shown in Table 5.1, the melting points of the SnAgCu and SnCu alloys are more than 30–40 °C higher than that of the eutectic SnPb alloy requiring the reflow.

The temperature for soldering components on assembly boards should be raised by 30–40 °C. The higher reflow

Table 5.1 Lead-free alloys

Alloy	Melting point
Sn96.5Ag3.5	221 °C
Sn96Ag3.5Cu0.5	217 °C
Sn20Au80	280 °C (mainly used in interconnects for optoelectronic packaging)
Sn99.3/Cu0.7	227 °C
SnAgCuX(Sb, in)	Ranging according to compositions, usually above 210 °C
SnAgBi	Ranging according to compositions, usually above 200 °C
Sn95Sb5	232–240 °C
Sn91Zn9	199 °C
SnZnAgAlGa	189 °C
Sn42Bi58	138 °C

temperature leads to a number of undesirable consequences such as higher residual stress of components and substrates, which adversely affects their reliability. It is also considered likely to have an increased tendency of the “pop-corning” found in the plastic-molded/plastic-encapsulated ICs during the reflow process. The high required temperature can potentially create serious warpage in organic board substrates. Furthermore, heat-sensitive components such as electrolytic capacitors might not survive the high process temperatures of lead-free assembly. Solders tend to be re-oxidized at high reflow temperatures, and the wettability becomes worsened

unless expensive nitrogen reflow is used. Therefore, industry's attentions have been paid on lowering the processing temperature of the lead-free metals.

The melting point of many materials can be dramatically reduced by decreasing the size of the materials. The melting and freezing behaviors of finite systems have been of considerable theoretical and experimental interests for many years. As early as 1888, J.J. Thomson suggested that the freezing temperature of a finite particle depends on the physical and chemical properties of the surface. It was not until 1909, however, that an explicit expression for a size-dependent solid–liquid coexistence temperature first appeared. By considering a system consisting of small solid and liquid spheres of equal mass in equilibrium with their common vapor, it was shown that the temperature of the triple point was inversely proportion to the particle size. A similar conclusion was later reached based on the conditions for equilibrium between a solid spherical core and a thin surrounding liquid shell. Systematic experimental studies of the melting and freezing behavior of small particles began to appear in the late 1940s and the early 1950s: first in a series of experiments on the freezing behavior of isolated micrometer-sized metallic droplets and second in an electron diffraction study of the melting and freezing temperatures of vapor-deposited discontinuous films consisting of nano-sized islands of Pb, Sn, and Bi. These studies demonstrated that small molten particles could often be dramatically undercooled and that solid particles melted significantly below their bulk melting temperature. To date, the melting point of substances can be dramatically decreased when their size is reduced to nanometer size [2–12]. This is due to the high surface area-to-volume ratio for nanoparticles, which as a consequence of the higher surface energy substantially affects the interior “bulk” properties of the material, resulting in a decrease of the melting point. The outer surface of the nanoparticles plays a relevant role in the melting point depression. And the surface premelting process has been suggested as one of the sources of the melting point depression of the nanoparticles [13].

Transmission electron microscopy (TEM) and nanocalorimeter have been used to study the melting behavior of a single Sn nanoparticle or cluster. At the melting point, the diffraction pattern of the crystal structure in TEM exhibited the order–disorder transition [14]. However, unlike calorimeters, TEM cannot measure the latent heat of fusion ($f.H_m$), which is very useful to understand the thermodynamics of a finite material system. Lai et al. investigated the melting process of supported Sn clusters by nanocalorimeter [3] and found that the melting point depended nonlinearly on the inverse of the cluster radius R , which was in contrast to the traditional description of the melting behavior of small

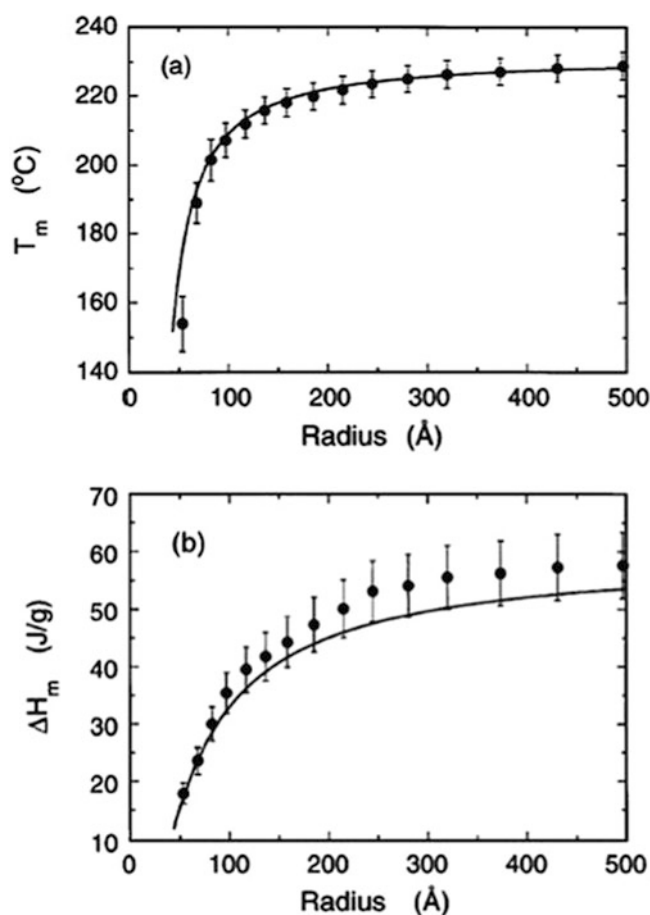


Fig. 5.2 (a) Size dependence of the melting points of Sn nanoparticles. The solid line is calculated in terms of Eq. (5.1). (b) Size dependence of the normalized heat of fusion. The solid line is calculated in terms of Eq. (5.2)

particles (Fig. 5.2a). They first reported a particle size-dependent reduction of $f.H_m$ for Sn nanoparticles (Fig. 5.2b). Bachels et al. studied the melting behavior of isolated Sn nanoparticles or clusters by nanocalorimeter as well [4]. The melting point of the investigated Sn clusters was found to be lowered by 125 K, and the latent heat of fusion per atom was reduced by 35% compared to bulk Sn. However, for both the TEM and nanocalorimetric measurements, the single element of Sn nanoparticle or the cluster was synthesized by the deposition method inside the measurement equipments in order to prevent the particles from oxidation.

Although this synthesis method was sufficiently sophisticated for the pure observation, the real-world synthesis and the characterization possess more experimental parameters to consider such as oxidation during moving samples and differences in melting/wetting behavior on different substrate materials.

$$T_m = 232 - 782 \left[\frac{\sigma_s}{15.8(r - t_0)} - \frac{1}{r} \right] \quad (5.1)$$

$$\Delta H_m = \Delta H_0 \left(1 - \frac{t_0}{r} \right)^3 \quad (5.2)$$

Various approaches to synthesize the single-element nanoparticles have been reported [41–43], which can be largely categorized into “bottom-up” (chemical reduction) and “top-down” methods (physical method). The chemical reduction methods include the inert gas condensation, sol-gel, aerosol, micelle/reverse micelle, and irradiation by UV, γ -ray, microwave, etc. [15–23]. For bimetallic or multicomponent nanoparticles, chemical “bottom-up” and physical “top-down” methods have also been used as well. The chemical methods use the coreduction of dissimilar metal precursors or successive reduction of two-metal salts, which is usually carried out to prepare a core-shell structure of bimetallic nanoparticles. The binary alloys reported in the form of nanoalloys or core-shell structures such as Ag–Au are an alloy system that forms solid solutions and their structures which can be controlled by the reduction order. On the other hand, in the case of alloys that do not favor the formation of solid solutions such as eutectic alloys (Sn-based alloys), little research has been reported because more sophisticated synthetic methods are required due to their oxidative nature. The physical method can be used to synthesize monometallic [24] and bimetallic nanoparticles [25]. Using this technique, nanoparticles can be synthesized in gram quantities directly from the bulk materials without complex reaction procedures. This is suitable for the low melting point metal precursors and their alloys.

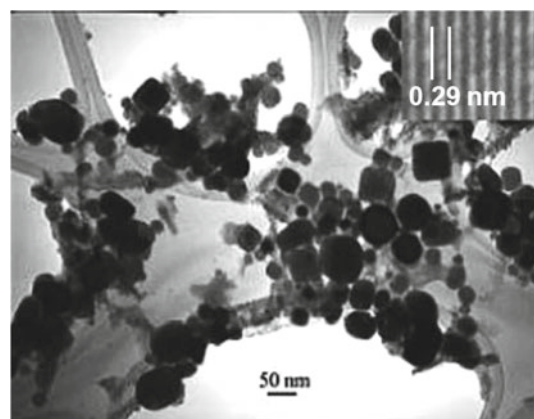
Duh et al. have reported Sn–3.5Ag– x Cu ($x = 0.2, 0.5, 1.0$) nanoparticle synthesis for the lead-free solder application [26], where the differential scanning calorimetry (DSC) profile showed the melting (endothermic) peak of their SnAgCu alloy nanoparticles at $\sim 216^\circ\text{C}$, which is the melting point of the micron meter-sized SnAgCu alloy powders. No obvious melting point depression from their particles might be due to the surface oxidation or heavy agglomeration of the nanoparticles.

Tin and its alloys are easily oxidized due to their low chemical potential. For nano-sized tin and its alloys, oxidation more easily happens due to the higher surface area-to-volume ratio of nanoparticles. However, the oxides of Sn and its alloys cannot form an interconnection between chips and substrates. Therefore, trapping each nanoparticle is critical for the prevention of oxidation, and capping agents/surfactants can cover the particle surfaces to serve as an effective barrier against the penetration of oxygen [44, 45]. Our research has found that some surfactant, such as 1,10-phenanthroline, is an effective capping agent on preventing tin and its alloy nanoparticles from oxidation.

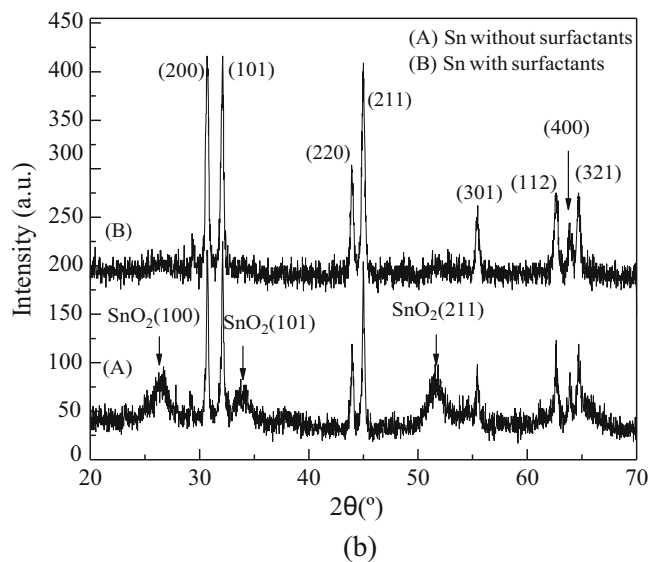
When Sn, SnAg, or SnAgCu alloy nanoparticles are formed, they are instantly coordinated to 1,10-phenanthroline through the two lone pair of chelating nitrogen donor sites adjoining to the two heterocyclic aromatic rings.

5.1 Size-Dependent Melting Point of Tin Nanoparticles

Figure 5.3a shows the TEM and inserted HRTEM images of Sn nanoparticles synthesized by using 2.1×10^{-4} mol tin (II) acetate as a precursor in the presence of 0.045 mol surfactants. The average particle size calculated from the TEM picture was around 61 nm, and the obvious lattice fringes in HRTEM image imply the crystalline structure. The interplanar spacing was about 0.29 nm which corresponds to the orientation of (200) atomic planes of the



(a)



(b)

Fig. 5.3 (a) TEM and inserted HRTEM images; (b) XRD of Sn nanoparticles which were synthesized by using 2.1×10^{-4} mol tin (II) acetate as a precursor in the presence of 0.045 mol surfactants

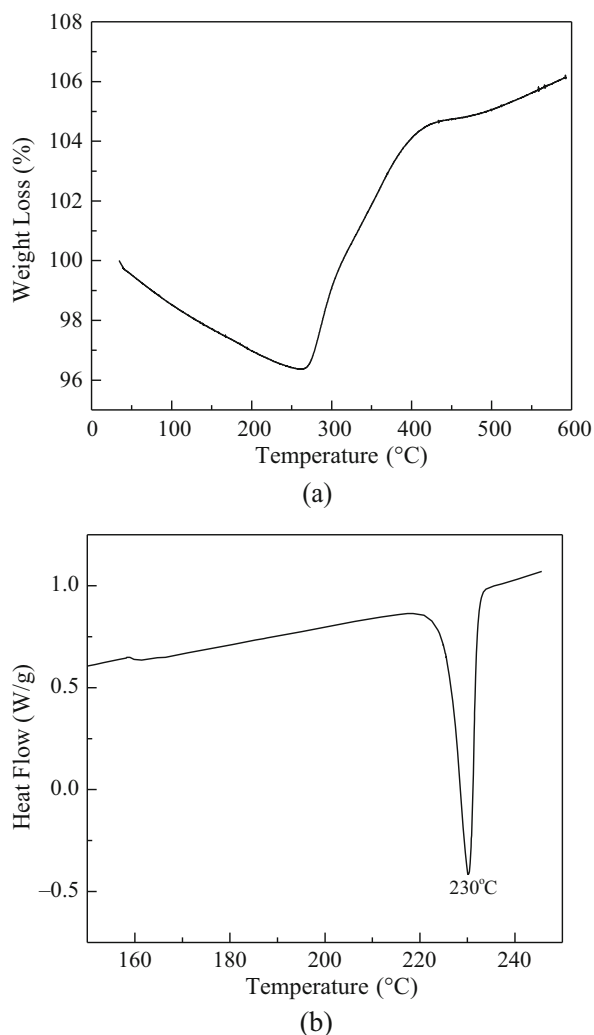


Fig. 5.4 TGA (a) and DSC (b) curves of the as-synthesized Sn nanoparticles

tetragonal structure of Sn. In the XRD pattern (Fig. 5.3b), all the peaks can be indexed to a tetragonal cell of Sn with $a = 0.582$ and $c = 0.317$ nm. The relative intensity of the peaks was consistent with that of the Sn nanoparticles reported elsewhere [27]. No obvious peaks at 20.6° , 33.8° , and 51.8° were found, which match the crystal planes of SnO₂: (100), (101), and (211) [28]. However, the obvious oxidation peaks of SnO₂ were observed from the X-ray diffraction (XRD) pattern of the Sn nanoparticles without surfactants. The XRD and high-resolution transmission electron microscopy (HRTEM) results showed that the Sn nanoparticles synthesized with surfactants in this study were nearly oxide-free.

Figure 5.4a shows the TGA curve of the as-synthesized Sn nanoparticles. The weight loss below 275°C may be due to the evaporation of absorbed moisture and the decomposition of the surfactants. Above 275°C , the weight gain was observed. This may be attributed to thermal oxidation of the

pure Sn nanoparticles. The TGA results showed that the Sn nanoparticles were covered with the surfactants by ~ 4 wt% to the particle weight. And these surfactants can protect the Sn nanoparticles from oxidation. Figure 5.4b shows the thermal profiles of the as-synthesized Sn nanoparticles obtained from DSC where the melting point (T_m) was observed at 230°C . Compared to the T_m of micron-sized Sn particles, the Sn nanoparticles exhibited the T_m depression by $2\text{--}3^\circ\text{C}$.

The oxide-free Sn nanoparticles were obtained by using the different molar ratios between a precursor and a surfactant. Thus, different-sized Sn nanoparticles can be obtained.

Figure 5.5a, b shows the TEM image and DSC profile of the Sn nanoparticles which were synthesized by using 4.2×10^{-4} mol tin (II) acetate as a precursor in the presence of 0.045 mol surfactants. The average particle size was around 52 nm. The melting point of the Sn nanoparticles was around 228.0°C , which was 4°C lower than that of micron-sized Sn particles. Figure 5.5c, d shows the TEM image and DSC profile of the Sn nanoparticles which were synthesized by using 1.1×10^{-3} mol tin (II) acetate as a precursor in the presence of 0.045 mol surfactants. The average particle size was around 85 nm. The melting point of the as-synthesized Sn nanoparticles was 231.8°C , which was still lower than the melting point of micron-sized Sn particles. The TEM image of Sn nanoparticles which were synthesized by using 1.75×10^{-4} mol tin (II) acetate as a precursor in the presence of 0.045 mol surfactants is shown in Fig. 5.5e. The average particle size was around 26 nm. The melting point of these particles was around 214.9°C , which was 17.7°C lower than that of micron-sized Sn particles. The melting transition of this sample took place over a temperature range of about 60°C , which was much wider than the other three samples. This phenomenon can be attributed to a broadening of the phase transition due to the finite size effect [29] and wide size distribution of the Sn nanoparticles. Schmidt et al. also found a melting temperature range of 60 K for cluster size with the number of atoms between 70 and 200 [8].

From Table 5.2, it can be seen that the larger molar ratios between the surfactants and the precursors were used, the smaller the particle size was. This is because a larger amount of surfactants can restrict the growth of Sn nanoparticles. The surfactant molecules coordinate with the nanoclusters, resulting in the capping effect to restrict the particle growth. This was also found by Pal et al. on their gold nanoparticle synthesis that increasing the concentrations of surfactants would limit the particle size through the restriction of particle growth [30]. The DSC results showed size-dependent melting depression behavior and size-dependent latent heat of fusion.

Figure 5.6 shows the size dependence of the melting points of the synthesized Sn nanoparticle powders, which was compared with Lai et al.'s model [3]. The solid line

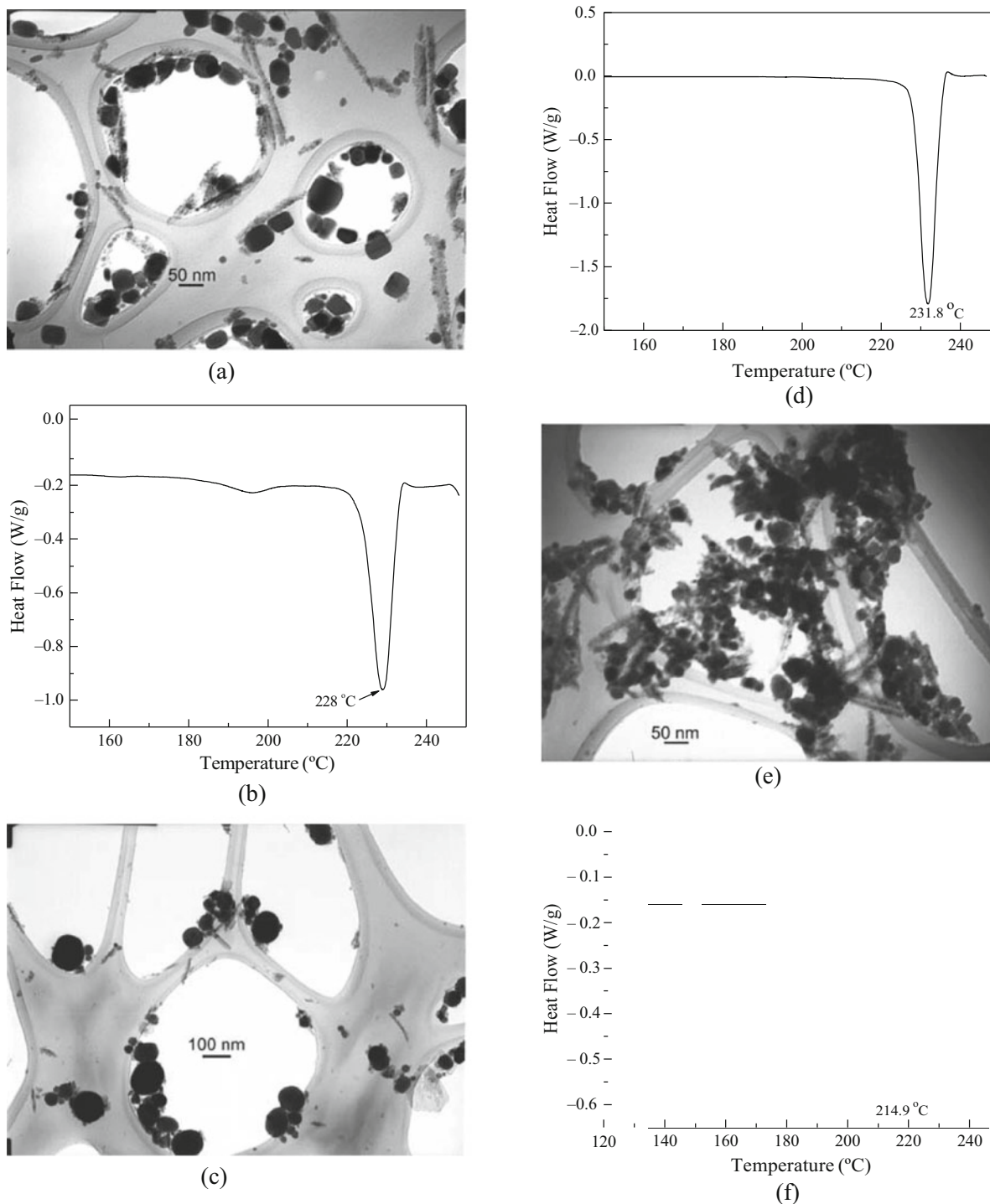


Fig. 5.5 TEM image and thermal behavior of Sn nanoparticles which were synthesized by using 4.2×10^{-4} mol (a) and (b), 1.1×10^{-3} mol (c) and (d), 1.75×10^{-4} mol (e) and (f) tin (II) acetate as a precursor in the presence of 0.045 mol surfactants

was calculated from Eq. (5.1). Lai et al. obtained this equation based on the model of Hanszen [31] in which it was assumed that the solid particle was embedded in a thin liquid

overlayer and the melting temperature was taken to be the temperature of equilibrium between the solid sphere core and the liquid overlayer of a given critical thickness t_0 .

Table 5.2 Melting points and heat of fusion of different-sized Sn nanoparticles

Samples	Surfactants/precursor	Average size (nm)	Melting point (°C)	$f..H$ (J/g)
1	N/A	Micron size	232.6	60.0
2	$0.045/1.1 \times 10^{-3}$	85 ± 10	231.8	32.1
3	$0.045/2.1 \times 10^{-4}$	61 ± 10	230.0	24.5
4	$0.045/4.2 \times 10^{-4}$	52 ± 8	228.0	28.7
5	$0.045/1.75 \times 10^{-4}$	26 ± 10	214.9	27.4

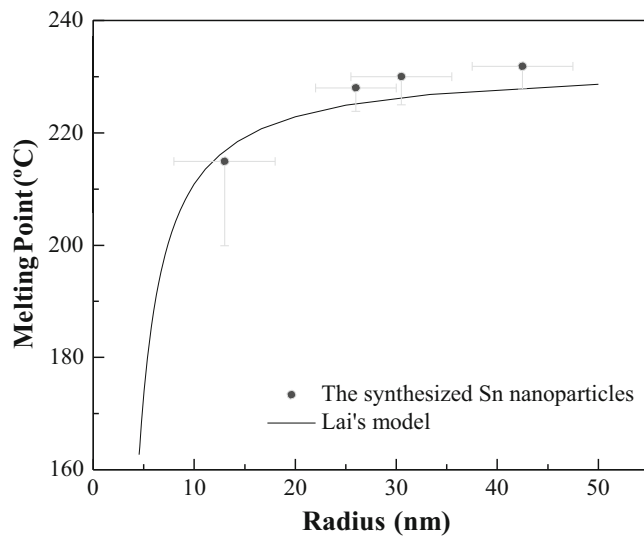


Fig. 5.6 Size dependence of the melting points of Sn nanoparticles (Y error bars stand for the melting temperature from the onset point to the peak point of DSC curves). The solid line is calculated from Eq. (5.1) by Lai et al. [3]

$$T_r = 232 - 782 \left[\frac{\sigma_{sl}}{15.8(r - t_0)} - \frac{1}{r} \right] \quad (5.3)$$

where T_r (°C) is the melting point of particles with a radius of r (Å), t_0 (Å) is the critical thickness of the liquid layer, and σ_{sl} is the interfacial surface tension between the solid and the liquid and the liquid and its vapor. From their experiment, σ_{sl} is determined to be 48 ± 8 mN/m and the best fit for t_0 is 18 Å.

It is found that our experimental results are in reasonable agreement with the Lai et al.'s model and the melting point depends nonlinearly on the cluster radius.

From Table 5.1, it could also be found that the latent heat of fusion of the different-sized Sn nanoparticles was smaller than that of micron-sized Sn powders. Ercolessi et al. have found that $f..Hm$ of gold nanoparticles decreases steadily from 114 meV/atom (bulk) to 23 meV/atom ($N = 879$) and 10 meV/atom ($N = 477$) by molecular dynamic simulation [32]. It is also found by experiments that the normalized heat of fusion of Sn nanoparticles decreases markedly from the bulk value (58.9 J/g) by as much as 70% when the particle

size is reduced, which can be interpreted as a solid core melting following the gradual surface melting for small particles [3]. We tried to compare the heat of fusion ($f..Hm$) of our synthesized Sn particles with Lai et al.'s model as well [3]. It was found that the $f..Hm$ values of our Sn particles were smaller than those of their models. This might be due to the existence of the surfactants, solvents, and some small amounts of oxides which might develop from the heating process of DSC test.

5.2 Size-Dependent Melting of Tin/Silver Alloy Nanoparticles

Figure 5.7a shows the TEM image of the SnAg alloy nanoparticles synthesized by using 7.4×10^{-4} mol tin (II) 2-ethylhexanoate and 3.0×10^{-5} mol silver nitrate as precursors in the presence of 5.6×10^{-4} mol surfactants at 0 °C. The average diameter of the particles was ~ 24.0 nm. The XRD patterns of the as-synthesized SnAg alloy nanoparticles are shown in Fig. 5.7b. In addition to the peaks indexed to a tetragonal cell of Sn with $a = 0.582$ and $c = 0.317$ nm, the Ag₃Sn phase ($\sim 39.6^\circ$) was found in the XRD patterns, indicating the successful alloying of Sn and Ag after the reduction process [26, 33]. No prominent oxide peak was observed from the XRD patterns. This indicates that the surfactants could help to protect the synthesized SnAg alloy nanoparticles from oxidation [34, 35].

Figure 5.8 shows the HRTEM image of the as-synthesized SnAg alloy nanoparticles, where the particles showed core-shell structures. The dark core and the brighter shell correspond to the crystalline metal and the amorphous organic surfactants, respectively. The surfactant shells on the particle surface protected the SnAg alloy nanoparticles from oxidation.

Figure 5.9a shows the TGA curve of the dried SnAg alloy nanoparticles in a nitrogen atmosphere. The weight loss below 180 °C might be due to the evaporation of a small amount of absorbed moisture and surfactants. Above 180 °C, the weight gain was observed, which was attributed to thermal oxidation of the SnAg alloy nanoparticles. Figure 5.9b displays the thermal profile of the dried SnAg alloy nanoparticles. The melting point of the SnAg nanoparticles was found at ~ 209.5 °C, about 13 °C lower than that of the

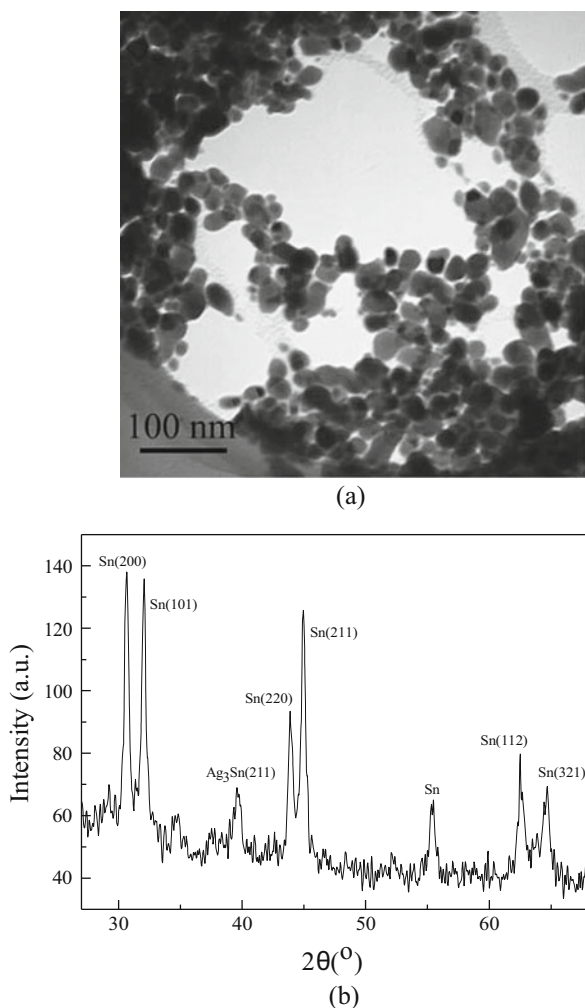


Fig. 5.7 The TEM image (a) and XRD patterns (b) of the SnAg alloy nanoparticles which were synthesized by using 7.4×10^{-4} mol tin (II) 2-ethylhexanoate and 3.0×10^{-5} mol silver nitrate as precursors in the presence of 5.6×10^{-4} mol surfactants

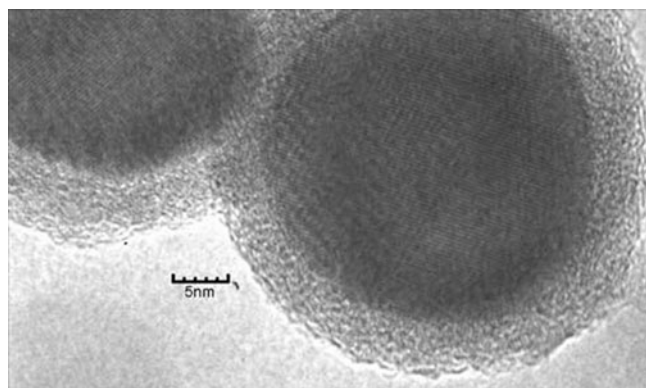


Fig. 5.8 HRTEM image of SnAg alloy nanoparticles which were synthesized by using 7.4×10^{-4} mol tin (II) 2-ethylhexanoate and 3.0×10^{-5} mol silver nitrate as precursors in the presence of 5.6×10^{-4} mol surfactants

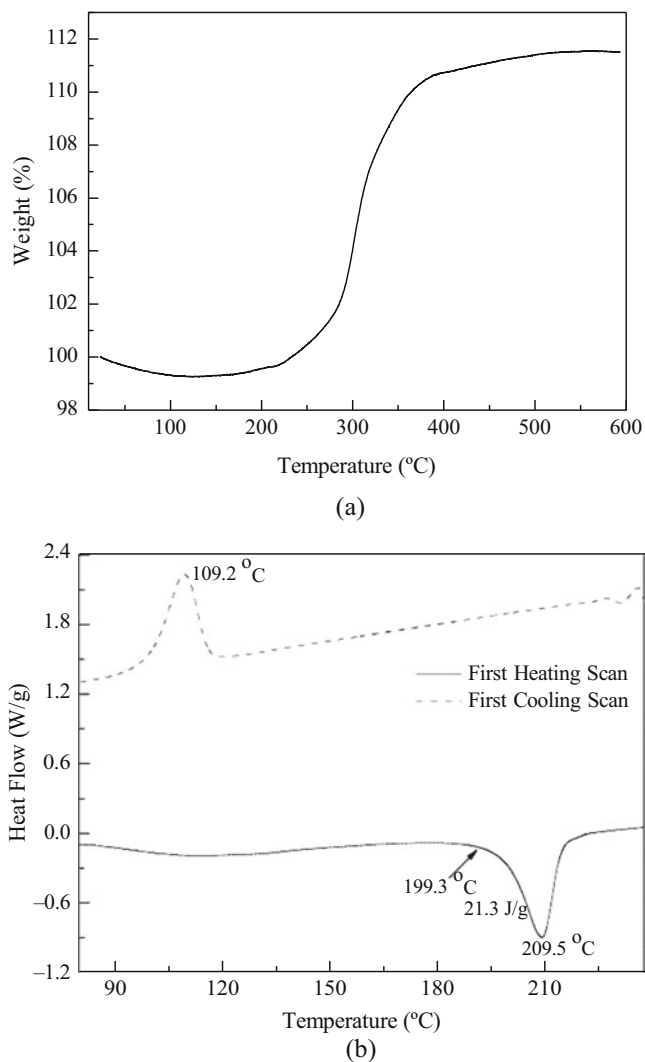
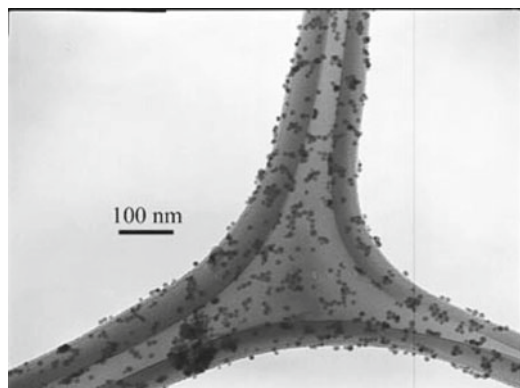


Fig. 5.9 The TGA (a) and DSC (b) curves of the SnAg alloy nanoparticles which were synthesized by using 7.4×10^{-4} mol tin (II) 2-ethylhexanoate and 3.0×10^{-5} mol silver nitrate as precursors in the presence of 5.6×10^{-4} mol surfactants

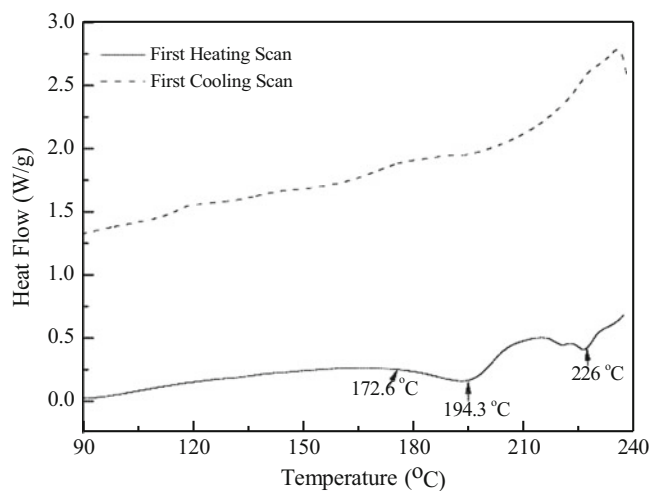
micron-sized 96.5Sn3.5Ag particles (222.6 °C). This was an obvious size-dependent melting point depression. The latent heat of fusion (*f.Hm*) of the SnAg alloy nanoparticles (24.2 J/g) was smaller than that of micron-sized 96.5Sn3.5Ag powders (68.6 J/g). It has already been observed by experiments that the normalized heat of fusion of Sn nanoparticles decreases markedly from the bulk value by as much as 70% when the particle size is reduced. This can be interpreted as a solid core melting following the gradual surface melting for small particles [3]. The recrystallization peak of the as-synthesized SnAg alloy nanoparticles was found at 109.2 °C, which was 91.2 °C lower than that of the micron-sized 96.5Sn3.5Ag particles (200.4 °C). Such a supercooling effect in the recrystallization of the melted Sn nanoparticles has already been observed [36], which can be

explained by the critical-sized stable grain that has to form for solidification to take place [37]. Solidification of the melted nanoparticles can only occur once the temperature is low enough so that the critical-sized solidification grain can be accommodated in a small volume.

The TEM image and the corresponding DSC curves of SnAg alloy nanoparticles which were synthesized by using 7.4×10^{-4} mol tin (II) 2-ethylhexanoate and 3.0×10^{-5} mol silver nitrate as precursors in the presence of 1.1×10^{-3} mol surfactants at 20 °C are shown in Fig. 5.10a, b. The average diameter of the as-synthesized nanoparticles was ~ 10 nm



(a)



(b)

Fig. 5.10 The TEM image (a) and DSC curves (b) of the SnAg alloy nanoparticles which were synthesized by using 7.4×10^{-4} mol tin (II) 2-ethylhexanoate and 3.0×10^{-5} mol silver nitrate as precursors in the presence of 1.1×10^{-3} mol surfactants

(Fig. 5.10a). From the DSC studies, the first peak melting temperature was 194.3 °C, which was about 28.3 °C lower than that of micron-sized 96.5Sn3.5Ag particles. The onset peak temperature was 172.6 °C, which was 46.9 °C lower than that of micron-sized particles (219.5 °C). The melting transition of this sample took place over a temperature range of about 21.7 °C, much wider than the micron-sized particles (3.1 °C). This phenomenon can be attributed to a broadening of the phase transition due to the finite size effect [29]. A small peak at 226.0 °C was also observed in the first heating scan, which might have come from the melting of a very small amount of larger-sized particles existing in this sample.

The melting point and latent heat of fusion for micron-sized 96.5Sn3.5Ag are 222.6 °C and 68.5 J/g, respectively.

Table 5.3 shows the melting point and latent heat of fusion of different-sized SnAg alloy nanoparticles. We plotted the melting point and $f.H_m$ vs. the corresponding particle radius in Fig. 5.11. Both the particle size-dependent melting point depression and latent heat of fusion have been observed. This is due to the surface premelting of nanoparticles. It has already been found that surface melting of small particles occurs in a continuous manner over a broad temperature range whereas the homogeneous melting of the solid core occurs abruptly at the critical temperature T_m [38, 39]. For smaller-sized metal nanoparticles, the surface melting is strongly enhanced by curvature effects. Therefore, with the decreasing of particle size, both the melting point and latent heat of fusion will decrease too. Among all the synthesized particles in Table 5.3, the 10 nm (average diameter) SnAg alloy nanoparticles have a melting point at ~ 194.3 °C, which will be a good candidate for the low melting temperature lead-free solders and can solve the issues from the high-temperature reflow for the micron-sized lead-free particles.

5.3 Size-Dependent Melting of Tin/Silver/Copper Alloy Nanoparticles

SnAgCu alloy nanoparticles were synthesized by a chemical reduction method. Figure 5.12 shows the TEM image of the as-synthesized SnAgCu alloy nanoparticles. It can be calculated that the average diameter of the particles is around 22 nm.

The XRD patterns of the as-synthesized SnAgCu alloy nanoparticles are shown in Fig. 5.13. In addition to the peaks

Table 5.3 The melting points and heat of fusion of the as-synthesized different-sized SnAg alloy nanoparticles

No.	Surfactants (mol)	Reaction temperature (°C)	Average diameter (nm)	Melting point (°C)	$f.H_m$ (J/g)
1	5.6×10^{-4}	25	64	220.0	44.7
2	5.6×10^{-4}	0	24	209.5	24.2
3	8.0×10^{-4}	10	17	206.0	15.1
4	1.1×10^{-3}	20	10	194.3	9.95

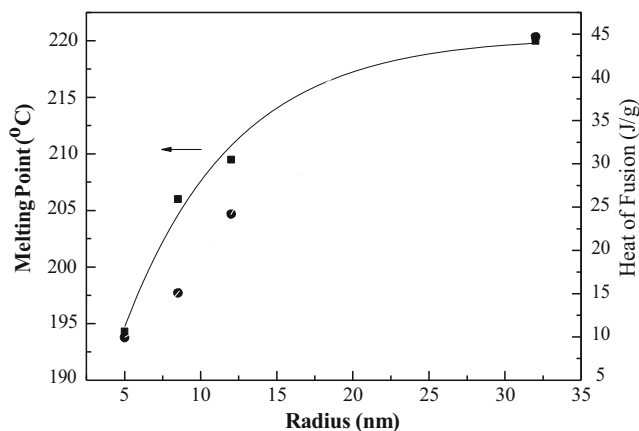


Fig. 5.11 The relationship between the radius of the as-synthesized SnAg alloy nanoparticles and their corresponding melting points and heat of fusion

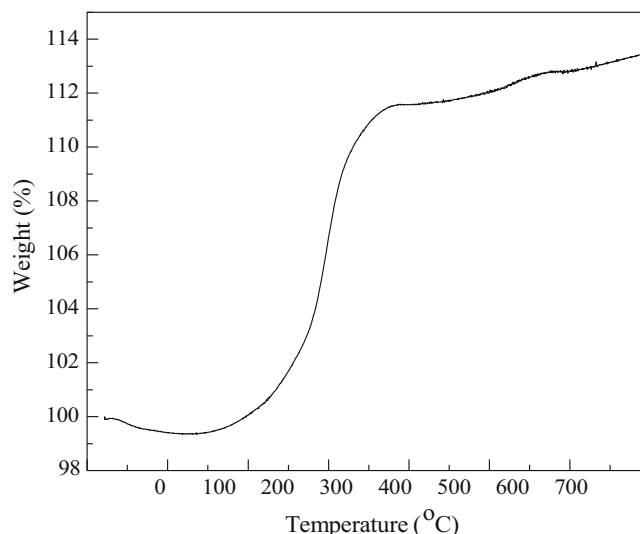


Fig. 5.14 The TGA curve of ~22 nm SnAgCu alloy nanoparticles

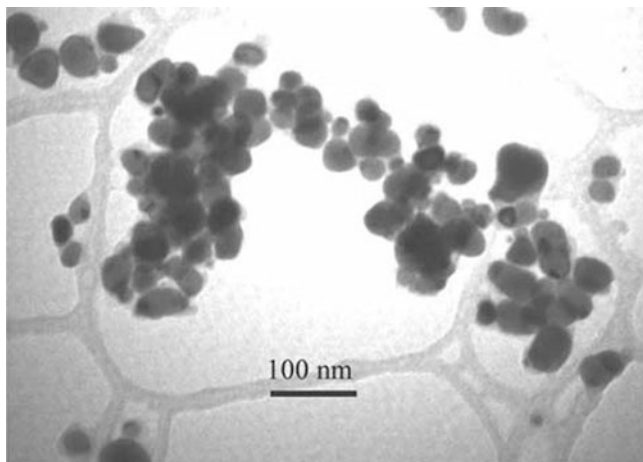


Fig. 5.12 The TEM image of ~22 nm SnAgCu alloy nanoparticles

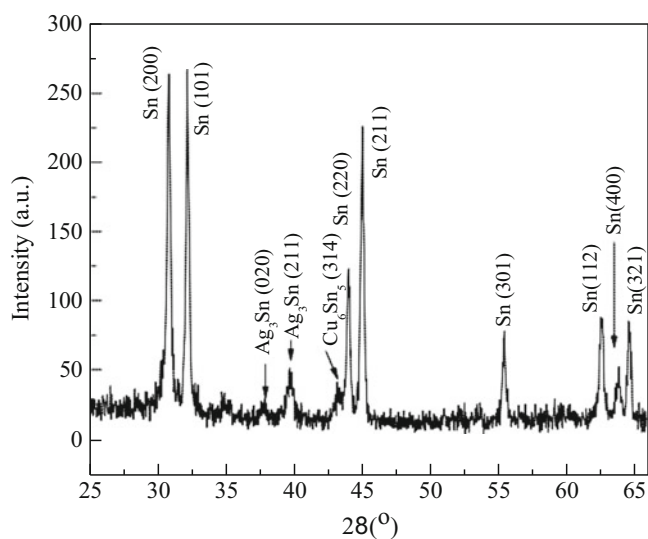


Fig. 5.13 The XRD patterns of ~22 nm SnAgCu alloy nanoparticles

indexed to a tetragonal cell of Sn with $a = 0.582$ and $c = 0.317$ nm, the Ag_3Sn phase (39.6°) was found in the XRD patterns, indicating the successful alloying of Sn and Ag after the reduction process [26, 33, 40].

At the same time, Cu_6Sn_5 was formed which was due to the alloying of Sn and Cu [26]. No prominent oxide peaks were observed from the XRD patterns. This indicates that surfactants can help protect the synthesized SnAgCu alloy nanoparticles from oxidation [34, 40]. The HRTEM characterizations already showed that the surfactants covered the particle surface and formed a core-shell structure [40]. The core was from the crystalline metal particles and the shell was from the amorphous surfactants. The amorphous surfactant shells on the particle surface helped prevent the diffusion of oxygen to SnAgCu alloy nanoparticles.

Figure 5.14 shows the TGA curve of the as-synthesized dried SnAgCu alloy nanoparticles in a nitrogen atmosphere. The weight loss below 180°C might be due to the evaporation or decomposition of a small amount of absorbed moisture and surfactants. Above 180°C , the weight gain was observed, which can be attributed to thermal oxidation of the SnAgCu alloy nanoparticles.

The thermal properties of the as-synthesized SnAgCu alloy nanoparticles were studied by a differential scanning calorimeter (Fig. 5.15). In the first heating scan of the DSC curve, an endothermic peak point at $\sim 207^\circ\text{C}$ was obtained, which is around $10\text{--}12^\circ\text{C}$ lower than the melting point of micron-sized SnAgCu ($217\text{--}219^\circ\text{C}$) alloy particles. In the first cooling scan, the supercooling of the nanoparticles with a crystallization peak at 113.3°C was observed, lower than that of micron-sized SnAgCu alloy nanoparticles (145°C). Such a supercooling effect in the recrystallization of the melted Sn and SnAg alloy nanoparticles has already been

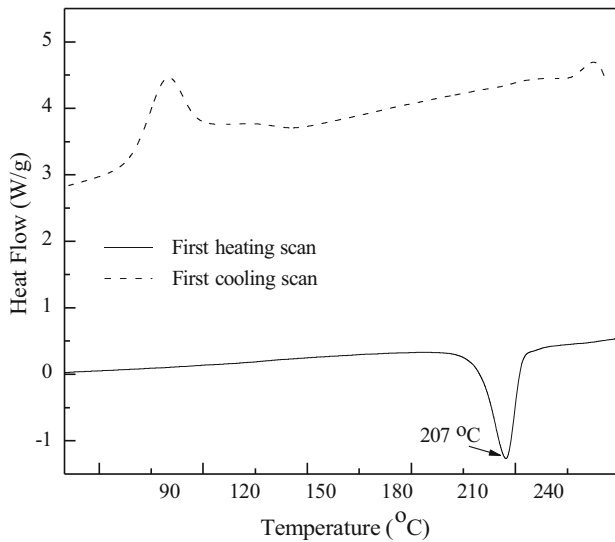
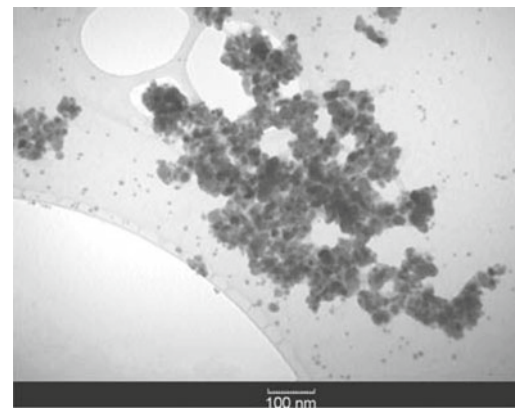


Fig. 5.15 The DSC curves of ~ 22 nm SnAgCu alloy nanoparticles

observed [36, 40], which can be explained by the critical-sized stable grain that needs to form in order for solidification to take place [37]. Solidification of the melted nanoparticles can only occur once the temperature is low enough so that the critical-sized solidification grain can be accommodated in a small volume.

Figure 5.16a shows the TEM image of 10–13 nm SnAgCu alloy nanoparticles which were synthesized by the chemical reduction method at a different reaction temperature. From DSC studies (Fig. 5.16b), the peak melting temperature was 199 °C, which was around 20 °C lower than that of micron-sized 96.5Sn3.0Ag0.5Cu particles. The onset peak temperature is 177 °C, 37.5 °C lower than micron-sized particles (214.5 °C). The melting transition of this sample took place over a temperature range of about 22 °C. This phenomenon can be attributed to broadening of the phase transition due to the finite size effect [29].

Table 5.4 shows the melting point, latent heat of fusion, and recrystallization temperature of different-sized SnAgCu alloy nanoparticles. Both size-dependent melting point depression and latent heat of fusion have been observed. It has already been found that surface melting of small particles occurs in a continuous manner over a broad temperature range whereas homogeneous melting of the solid core occurs abruptly at the critical temperature T_m [39]. For smaller-sized metal nanoparticles, surface melting is strongly enhanced by the curvature effects. Therefore, with the decrease of particle size, both the melting point and latent heat of fusion decrease as well. Among all the synthesized particles in Table 5.4, the 10–13 nm (average diameter) SnAgCu alloy nanoparticles have the lowest melting point at ~ 199 °C, indicating it to be a good candidate for lead-free solders as its melting point is



(a)

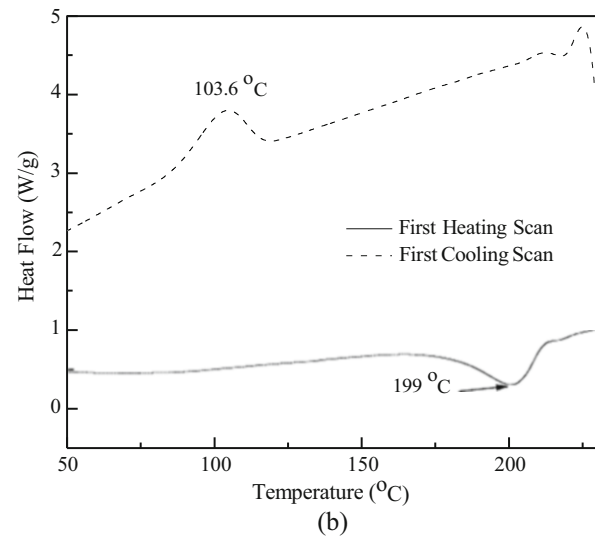


Fig. 5.16 The TEM image (a) and DSC curves (b) of 10–13 nm SnAgCu alloy nanoparticles

Table 5.4 The melting and recrystallization points, heat of fusion of different-sized SnAgCu alloy nanoparticles

Size	Melting point (°C)	<i>f.H</i> (J/g)	Recrystallization (°C)
Micron	217	72.2	145
~ 28 nm	210.4	42.7	112.3
~ 22 nm	207.3	31.0	109.9
~ 18 nm	206.1	24.7	108.7
~ 10 –13 nm	199	15.9	103.6

comparable to the reflow temperature of the conventional eutectic micron-sized SnPb alloy particles.

5.4 Wetting Properties of Tin/Silver and Tin/Silver/Copper Alloy Nanoparticle Pastes

The solder paste is a viable interconnecting material, providing electrical, thermal, and mechanical properties applicable to electronics assemblies. It is a homogeneous

and kinetically stable mixture of solder alloy powder, flux, and vehicle, which is capable of forming metallurgical bonds at given soldering conditions (Fig. 5.17).

Solder alloy powders are usually tin/lead (SnPb), lead-free solder materials, such as tin/silver (SnAg), tin/silver/copper (SnAgCu), and tin/copper (SnCu). The flux can cause the alloy powders and the surfaces to be joined to maintain a clean and metallic state. The vehicle is a carrier for the solder powder, provides a desirable rheology, and protects the molten solder and the cleaned substrates from re-oxidation.

The elements used in solder alloys are tin, lead, silver, copper, bismuth, indium, antimony, and cadmium. Phase diagram can be used to determine the eutectic point and the corresponding compositions for the solid solution. Several methods can be used to make the solder alloy powders, such as chemical reduction, decomposition, mechanical processing of solid metal, and atomization of liquid metals. Chemical reduction method and decomposition can be used to prepare fine solder alloy particles. Mechanical processing of solder metal can be used to prepare flake-like particles, while powders to be used in a solder paste are mostly produced by atomization because of desirable inherent morphology and shape of resulting particles.

Melting range, flow rate, and particle morphologies are important parameters for solder powders. The melting range

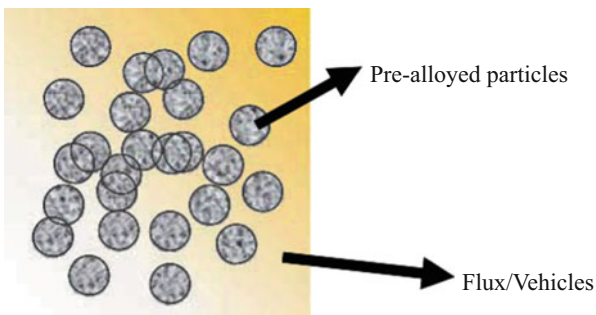


Fig. 5.17 The composition of solder pastes

of solder powders is usually tested by differential scanning calorimetry (DSC). Table 5.1 shows the melting point of SnPb solders and lead-free solders. The particle size, size distribution, and shapes are usually tested by scanning electron microscopy (SEM), light scattering, and so on.

Some of the other physical properties, like viscosity, surface tension, thermal properties, electrical properties, and thermal expansion coefficient, are also very important for the solder materials. For the SnPb alloys, the surface tension and thermal and electrical conductivity decrease with increasing lead content, while viscosity and thermal expansion coefficient increase with increasing lead content.

The function of fluxes in a solder paste is to chemically clean the surfaces to be joined, to clean the surface of solder powder, and to maintain the cleanliness of both substrate surface and solder powder surface during reflow so that a metallic continuity at the interface and a complete coalescence of the solder powder during reflow can be achieved (Fig. 5.18).

There are several kinds of fluxes:

- Type R-rosin flux, the weakest, contains only rosin without the presence of activator.
- Type RMA (mildly activated rosin) is a system containing both rosin and activator.
- Type RA is a fully activated rosin and resin system, having a higher flux strength than the RMA type.
- Type OA is an organic acid flux and possessing a high fluxing activity and is generally considered corrosive.
- Type SA (synthetic activator) is designed to improve the fluxing activity on hard-to-solder surfaces. The SA flux displays better wetting ability than RA flux and is equivalent to OA flux.

The major components of unmodified rosin are abietic acid, isopimaric acid, neoabietic acid, pimaric acid, dihydroabietic acid, and dehydroabietic acid. The chemical structures of these acids are shown in Fig. 5.19.

Fig. 5.18 The function of flux

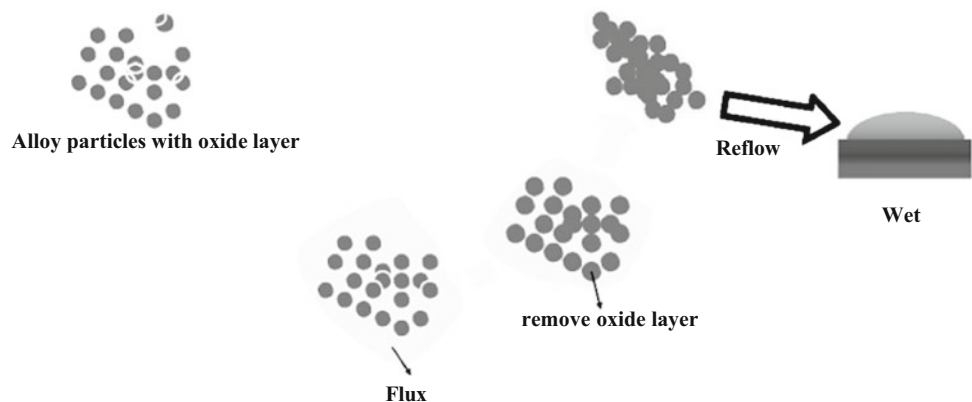


Fig. 5.19 The chemical structures of the acids in rosin

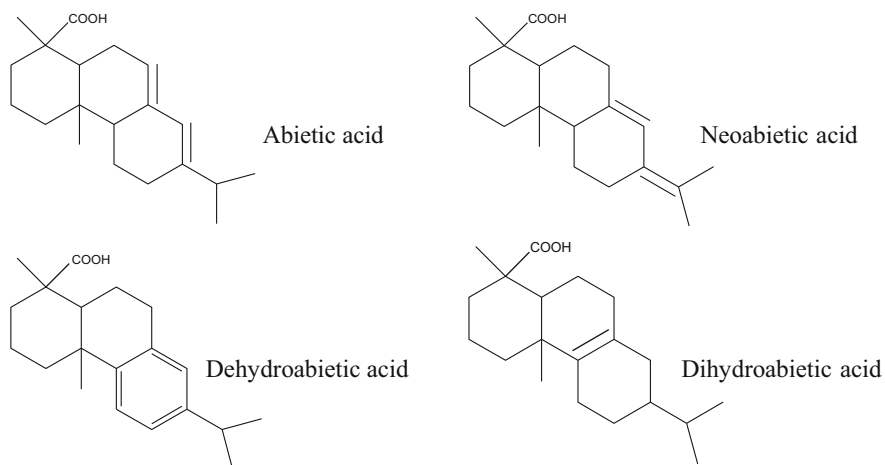
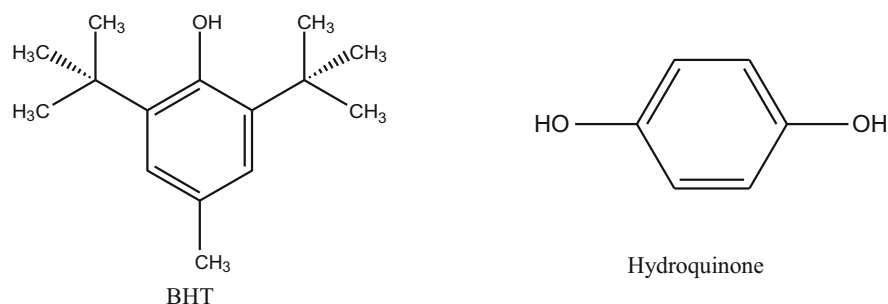


Fig. 5.20 The chemical structures of BHT and hydroquinone



The main compositions of vehicles we used in this section are tackifier, solvent, antioxidation agent, and surfactants.

The tackifier is typically a medium-to-high viscosity, high surface tension liquid serving to wet the printed circuit board and the component and retain the component in position during handling and reflow soldering. The tackifier usually comprises one or more alcohols, aromatic hydrocarbon solvents, aliphatic hydrocarbon solvents, or polymers.

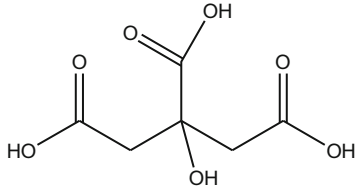
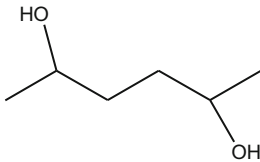
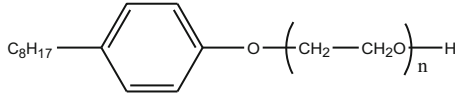
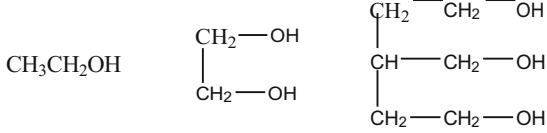
A suitable solvent vehicle includes any solvent which is chemically inert with the other components in the flux. Three important parameters for solvents are boiling point, viscosity, and polarity. Alcohols are usually used as solvents. The more hydroxyl groups the solvents have, the better activity the flux will have.

Antioxidation agents are used to protect the Sn and its alloy nanoparticles from oxidation. Butylated hydroxytoluene (BHT) and hydroquinone (Fig. 5.20) are the typically used antioxidation agents. Oxygen reacts preferentially with BHT or hydroquinone rather than oxidizing Sn alloy, thereby protecting them from oxidation.

The solder surfactant is a compound which improves the solder wetting rate of a surface and enables better and more uniform spreading of molten solder across the surface to be soldered. Suitable surfactants include polybasic acids, e.g., polycarboxylic acids such as dicarboxylic and tricarboxylic acids. The dibasic acids typically have 4–10 carbon atoms. Suitable tricarboxylic acids typically comprise acids having 6–7 carbon atoms. Other suitable surfactants include hydroxyl-substituted polybasic acids, such as tartaric acid and citric acid. The selected surfactant is present in the flux mixture in an amount of at least 1 wt% of the resultant flux mixture.

The solderability, flow properties, wetting properties, and solidification are important physical properties for the solder pastes. Solderability is the ability to achieve a clean, metallic surface on solder powder and on substrates during the dynamic heating process so that a complete coalescence of solder powder particles and good wetting of molten solder on the surface of the substrates can be formed. Solderability

Table 5.5 The composition of flux and vehicle made by our group

Fluxing agent	
Tackifier	
Surfactant	
Solvent	
Antioxidation	BHT

depends on fluxing efficiency by the solder pastes and the quality of surface of substrates.

When heat is applied to the paste through any means, the paste tends to spread or slump due to gravity and thermal energy generated. The surface energies of the liquid and the solid substrates are key factors in determining the spreading and wetting properties. For a system with liquid to wet the solid substrate, the spreading occurs only if the surface energy of the substrate to be wetted is higher than that of the liquid to be spread.

The solidification of liquid metal occurs by nucleation and crystal growth. Dendritic growth during solidification is a common phenomenon in pure metals and alloys. The heat flow during the solidification and the crystal structure of the alloy are crucial factors to the properties and structure of the solidified alloy.

Application techniques for the solder pastes usually include printing and paste dispensing. Printing is a viable method to economically produce accurate and reproducible transfer of paste onto the designed pattern, but only suitable for a flat surface. However, paste dispensing can be used for irregular surface or hard-to-reach area.

Conduction reflow is most suitable for the assemblies with flat surfaces, composed of thermal conductive materials as the substrates and with single-side component/device populations (fast heating rate and operational simplicity). Infrared reflow is a dynamic process. The precise temperature profile depends on solder alloy composition, properties of the

pastes, and assembly involved. Some other reflow methods, such as vapor phase reflow, convection reflow, hot gas reflow, resistance reflow, laser reflow, and induction reflow, are also being used.

Residue is composed of polar organics, nonpolar organics, ionic salts, and metal salts of organics. The cleaning solvents include trichlorotrifluoroethane, 1,1,1-trichloroethane, acetone, methylene chloride, low carbon-chain alcohols, and water. Basic techniques include vapor degreasing, liquid spray, liquid immersion, high-pressure spray, and liquid immersion with ultrasonic acid.

A certain amount of fluxing agent, solvent, antioxidation agent, surfactants, and tackifier was mixed together to prepare the flux and vehicle for the SnAg or SnAgCu alloy nanoparticles. Table 5.5 shows the composition of the flux and vehicle we made and their corresponding chemical structures.

The SnAg alloy nanoparticles (sample 1 in Table 5.3) were mixed with an acidic-type flux to form the nanosolder pastes at room temperature. A copper foil was cleaned by hydrochloric acid to get rid of the oxide layer and then rinsed with DI water for four times. Thereafter, the nanosolder pastes placed on top of the copper foil were put into a 230 °C oven in an air atmosphere for 5 min. The cross section of the sample after reflow was shown in Fig. 5.21. It was observed that the SnAg alloy nanoparticles completely melted and wetted on the cleaned copper foil surface. The energy-dispersive spectroscopy (EDS) results revealed the

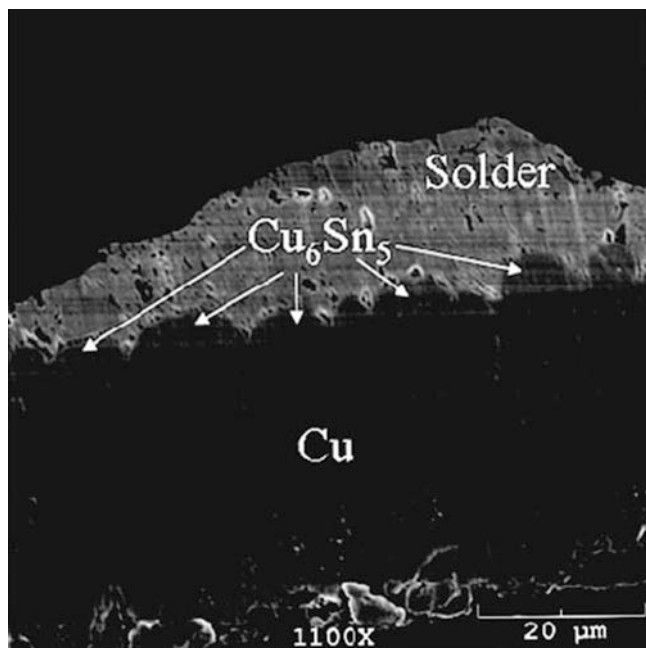


Fig. 5.21 SEM image of the cross section of the wetted SnAg alloy nanoparticles (sample 1 in Table 5.3) on the cleaned copper foil [46]

formation of the intermetallic compound (IMC) of Cu_6Sn_5 , which showed scallop-like morphologies in Fig. 5.21. The thickness of the IMC was approximately $4.0 \mu\text{m}$. Further studies on the wetting properties of different-sized SnAg alloy nanoparticles at different reflow temperatures are still ongoing.

Nanolead-free solder pastes were formed by dispersing the synthesized SnAgCu alloy nanoparticles into the flux and vehicle system. Carboxylic acid was used as the fluxing agent. The vehicle system mainly consists of a tackifier, a surfactant, solvents, antioxidation agents, etc. The tackifier is typically a medium-to-high viscosity, high surface tension liquid serving to wet the printed circuit board and the component and retain the component in position during the handling and reflowing process. The surfactant is a compound which enables better and more uniform spreading of molten solder across the surface to be soldered. The antioxidation agents were used to protect the molten solder and substrates from oxidation.

A copper foil was cleaned by hydrochloric acid to get rid of the oxide layer and then rinsed with DI water for four times. Thereafter, the $\sim 50 \text{ nm}$ (average diameter) SnAgCu alloy nanoparticle pastes placed on top of the copper foil were put into a 220°C oven in an air atmosphere for 5 min. The cross section of the sample after reflow was shown in Fig. 5.22. It was observed that the SnAgCu alloy nanoparticles completely melted and wetted on the cleaned copper foil surface. The energy-dispersive spectroscopy (EDS) results revealed the formation of the intermetallic

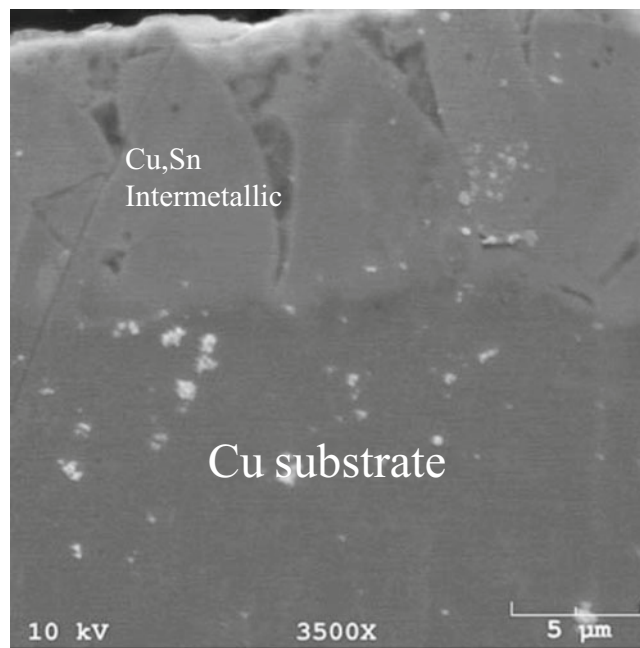


Fig. 5.22 SEM image of the cross section of the wetted 50 nm SnAgCu alloy nanoparticles on copper foil

compounds (Cu_6Sn_5), which showed scallop-like morphologies in Fig. 5.22. The thickness of intermetallic compounds was approximately $10.0 \mu\text{m}$. The wetting properties of different-sized SnAgCu alloy nanoparticles at different reflow temperatures need to be further studied.

5.5 Conclusion

This chapter addresses the synthesis routes for lead-free nanoparticles including a tin single element and alloys and their structures and thermal behavior based on melting point depression. During this study, we observed obvious melting point depression behavior of synthesized nanoparticles and learned, most of all, that the surface oxidation of the non-noble nanoparticle is a critical obstacle in the case where melting of the particles is needed. Therefore, we found the surface capping by functionalization was imperative and when and how the surface can be capped were very important factors to obtain oxide-free non-noble metal nanoparticles, together with the careful selection of the surfactant. Finally in order to make nanosolder pastes, the appropriate flux vehicle and the reflow profile optimization were very important, which are also the lessons we learned.

The aim of this study is the reduction of the reflow temperature in microelectronic packaging processes which may be a representative case study to employ cutting-edge nanoscience and technology into the real-world research and development arena.

References

- Abtew, M., Selvaduray, G.: Lead-free solders in microelectronics. *Mater. Sci. Eng. R. Rep.* **27**, 95 (2000)
- Wronski, C.R.M.: Size dependence of melting point of small particles of tin. *Br. J. Appl. Phys.* **18**, 1731 (1967)
- Lai, S.L., Guo, J.Y., Petrova, V., Ramanath, G., Allen, L.H.: Size-dependent melting properties of small tin particles: nanocalorimetric measurements. *Phys. Rev. Lett.* **77**(1), 99–102 (1996)
- Bachels, T., Guntherodt, H.J., Schafer, R.: Melting of isolated tin nanoparticles. *Phys. Rev. Lett.* **85**(6), 1250–1253 (2000)
- Zhao, S.J., Wang, S.Q., Cheng, D.Y., Ye, H.Q.: Three distinctive melting mechanisms in isolated nanoparticles. *J. Phys. Chem. B.* **105**(51), 2857–12860 (2001)
- Shvartsburg, A., Jarrold, M.F.: Solid clusters above the bulk melting point. *Phys. Rev. Lett.* **85**, 2530 (2000)
- Cleveland, L., Luedtke, W.D., Landman, U.: Melting of gold clusters: icosahedral precursors. *Phys. Rev. Lett.* **81**, 2036 (1998)
- Schmidt, M., Kusche, R., Issendorff, B., Haberland, H.: Irregular variations in the melting point of size-selected atomic clusters. *Nature.* **393**(6682), 238–240 (1998)
- Lewis, L.J., Jensen, P., Barrat, J.L.: Melting, freezing, and coalescence of gold nanoclusters. *Phys. Rev. B.* **56**, 2248 (1997)
- Cleveland, C.L., Landman, U., Luedtke, W.D.: Phase coexistence in clusters. *J. Phys. Chem.* **98**, 6272 (1994)
- Shi, F.G.: Size-dependent thermal vibrations and melting in nanocrystals. *J. Mater. Res.* **9**, 1307 (1994)
- Jiang, Q., Shi, F.G.: Entropy for solid-liquid transition in nanocrystals. *Mater. Lett.* **37**, 79 (1998)
- Allen, L., Bayles, R.A., Gile, W.W., Jesser, W.A.: Small particle melting of pure metals. *Thin. Solid. Film.* **144**, 297 (1986)
- Buffat, P., Borel, J.P.: Size effect on melting temperature of gold particles. *Phys. Rev. A.* **13**, 2287 (1976)
- Birringer, R., Gleiter, H., Klein, H.P., Marquart, P.: Nanocrystalline materials an approach to a novel solid structure with gas-like disorder? *Phys. Lett.* **102A**, 365 (1984)
- Lee, B.I., Pope, E.J.A.: *Chemical Processing of Ceramics*. Marcel Dekker, New York (1994)
- Raabe, O.G.: In: Liu, B.Y.H. (ed.) *Fine Particles*, p. 60. Academic, New York (1975)
- J. P. Wilcoxon, A. Martino, R. L. Baughmann, E. Klavetter, A. P. Sylwester, “Synthesis of transition metal clusters and their catalytic and optical properties”, in “Nanophase and Nanocomposite Materials” S. Komarneni, J. C. Parker and G. J. Thomas, MRS, Pittsburgh, 1993: p. 131
- Thomas, J.: Preparation and magnetic properties of colloidal cobalt particles. *J. Appl. Phys.* **37**, 2914 (1966)
- Rochfort, G.L., Rieke, R.D.: Preparation, characterization, and chemistry of activated cobalt. *Inorg. Chem.* **25**, 348 (1986)
- Koch, C.C.: Materials synthesis by mechanical alloying. *Ann. Rev. Mater. Sci.* **19**, 121 (1989)
- Klabunde, K., Li, Y., Tan, B.: Solvated metal atom dispersed catalysts. *Chem. Mater.* **3**, 30 (1991)
- Mafune, F., Kohno, J.Y., Takeda, Y., Kondow, T.: Dissociation and aggregation of gold nanoparticles under laser irradiation. *J. Phys. Chem. B.* **105**, 9050 (2001)
- Zhao, Y.B., Zhang, Z.J., Dang, H.X.: Preparation of tin nanoparticles by solution dispersion. *Mater. Sci. Eng.* **A359**, 405 (2003)
- Zhao, Y.B., Zhang, Z.J., Dang, H.X.: Synthesis of In-Sn alloy nanoparticles by a solution dispersion method. *J. Mater. Chem.* **14**, 299 (2004)
- Hsiao, L.Y., Duh, J.G.: Synthesis and characterization of lead-free solders with Sn-3.5Ag- xCu (x=0.2, 0.5, 1.0) alloy nanoparticles by the chemical reduction method. *J. Electrochem. Soc.* **152**(9), J105–J109 (2005)
- Kwon, Y., Kim, M.G., Kim, Y., Lee, Y., Cho, J.: Effect of capping agents in tin nanoparticles on electrochemical cycling. *Electrochem. Solid-State Lett.* **9**, A34 (2006)
- Wang, Y., Lee, J.Y., Deivaraj, T.C.: Controlled synthesis of V-shaped SnO₂ nanorods. *J. Phys. Chem. B.* **108**, 13589 (2004)
- Imry, Y., Bergman, D.: Critical points and scaling laws for finite systems. *Phys. Rev. A.* **3**(4), 1416 (1971)
- Mandal, M., Ghosh, S.K., Kundu, S., Esumi, K., Pal, T.: UV photoactivation for size and shape controlled synthesis and coalescence of gold nanoparticles in micelles. *Langmuir.* **18**, 7792 (2002)
- Hanszen, K.J.: Theoretische untersuchungen uber den schmelzpunkt kleiner kugelchen – Ein beitrag zur thermodynamik der grenzflächen. *Z. Phys.* **157**, 523–553 (1960)
- Ercolessi, F., Andreoni, W., Tosatti, E.: Melting of small gold particles – mechanism and size effects. *Phys. Rev. Lett.* **66**(7), 911–914 (1991)
- Lai, H.L., Duh, J.G.: Lead-free Sn-Ag and Sn-Ag-Bi solder powders prepared by mechanical alloying. *J. Electron. Mater.* **32**(4), 215–220 (2003)
- Jiang, H.J., Moon, K., Dong, H., Hua, F., Wong, C.P.: Size-dependent melting properties of tin nanoparticles. *Chem. Phys. Lett.* **429**, 492–496 (2006)
- Balan, L., Schneider, R., Billaud, D., Ghanbaja, J.: A new organometallic synthesis of size-controlled tin(0) nanoparticles. *Nanotechnol.* **16**(8), 1153–1158 (2005)
- Banhart, F., Hernandez, E., Terrones, M.: Extreme superheating and supercooling of encapsulated metals in fullerene-like shells. *Phys. Rev. Lett.* **20**(18), 185502 (2003)
- Christenson, H.K.: Confinement effects on freezing and melting. *J. Phys. Condens. Matter.* **13**(11), R95–R133 (2001)
- Garrigos, R., Cheyssac, P., Kofman, R.: Melting of lead particles of small sizes – influence of surface phenomena. *Z. Phys. D.* **12**, 497 (1989)
- Hu, W.Y., Xiao, S.G., Yang, J.Y., Zhang, Z.: Melting evolution and diffusion behavior of vanadium nanoparticles. *Eur. Phys. J. B.* **45**(4), 547–554 (2005)
- Jiang, H., Moon, K., Hua, F., Wong, C.P.: Synthesis and thermal and wetting properties of tin/silver alloy nanoparticles for low-melting point lead-free solders. *Chem. Mater.* **9**(8), 4482–4485 (2007)
- Jiang, H., Moon, K., Sun, Y., Wong, C.P., Hua, F., Pal, T., Pal, A.: Tin/indium nanobundle formation from aggregation or growth of nanoparticles. *J. Nanopart. Res.* **10**(1), 41–46 (2008)
- Jiang, H., Zhu, L., Moon, K., Wong, C.P.: The preparation of stable metal nanoparticles on carbon nanotubes whose surface were modified during production. *Carbon.* **45**(3), 655–661 (2007)
- Jiang, H., Moon, K., Zhang, Z., Pothukuchi, S., Wong, C.P.: Variable frequency microwave synthesis of silver nanoparticles. *J. Nanopart. Res.* **8**(1), 117–124 (2006)
- Jiang, H., Moon, K., Li, Y., Wong, C.P.: Surface functionalized silver nanoparticles for ultra-highly conductive polymer composites. *Chem. Mater.* **18**(13), 2969–2973 (2006)
- Jiang, H., Moon, K., Lu, J., Wong, C.P.: Conductivity enhancement of nano Ag filled conductive adhesives by particle surface functionalization. *J. Electron. Mater.* **34**(11), 1432–1439 (2005)
- Jiang, H., Moon, K., Wong, C.P.: Tin/silver/copper alloy nanoparticles for low temperature solder pastes interconnect. In: *IEEE 58th Electronic Components & Technology Conference*, May 27–30, 2008, pp. 1400–1404 (2008)